Journal of Energy Chemistry 40 (2020) 120–131

Contents lists available at ScienceDirect

Journal of Energy Chemistry

journal homepage: www.elsevier.com/locate/jechem

http://www.journals.elsevier.com/journal-of-energy-chemistry/

Fabrication and study of supercapacitor electrodes based on oxygen plasma functionalized carbon nanotube fibers

Paa Kwasi Adusei[a], Seyram Gbordzoe[a], Sathya Narayan Kanakaraj[a], Yu-Yun Hsieh[a], Noe T. Alvarez[c], Yanbo Fang[a], Kevin Johnson[b], Colin McConnell[a], Vesselin Shanov[a,b,*]

[a] Department of Mechanical and Materials Engineering, University of Cincinnati, Cincinnati, OH 45221-0072, USA
[b] Department of Chemical and Environmental Engineering, University of Cincinnati, OH 45221-0012, USA
[c] Department of Chemistry, University of Cincinnati, OH 45221-0172, USA

ARTICLE INFO

Article history:
Received 27 December 2018
Revised 4 March 2019
Accepted 5 March 2019
Available online 12 March 2019

Keywords:
Oxygen plasma functionalization
Fiber supercapacitors
CNT fiber electrodes
Ionic liquid

ABSTRACT

Dry-spun Carbon Nanotube (CNT) fibers were surface-modified by atmospheric pressure oxygen plasma functionalization using a well controlled and continuous process. The fibers were characterized by scanning electron microscopy (SEM), Raman spectroscopy, and X-ray Photoelectron Spectroscopy (XPS). It was found from the conducted electrochemical measurements that the functionalized fibers showed a 132.8% increase in specific capacitance compared to non-functionalized fibers. Dye-adsorption test and the obtained Randles-Sevcik plot demonstrated that the oxygen plasma functionalized fibers exhibited increased surface area. It was further established by Brunauer-Emmett-Teller (BET) measurements that the surface area of the CNT fibers was increased from 168.22 m^2/g to 208.01 m^2/g after plasma functionalization. The pore size distribution of the fibers was also altered by this processing. The improved electrochemical data was attributed to enhanced wettability, increased surface area, and the presence of oxygen functional groups, which promoted the capacitance of the fibers. Fiber supercapacitors were fabricated from the oxygen plasma functionalized CNT fiber electrodes using different electrolyte systems. The devices with functionalized electrodes exhibited excellent cyclic stability (93.2% after 4000 cycles), flexibility, bendability, and good energy densities. At 0.5 mA/cm^2, the EMIMBF4 device revealed a specific capacitance, which is 27% and 65% greater than the specific capacitances of devices using EMIMTFSI and H_2SO_4 electrolytes, respectively. The practiced in this work plasma surface processing can be employed in other applications where fibers, yarns, ribbons, and sheets need to be chemically modified.

1. Introduction

Flexible and bendable electronic devices have become of much interest, especially for wearable electronics. Amongst them, fiber devices present several advantages over their conventional counterparts. They are lightweight, can be seamlessly integrated into textile, and have a high surface to volume ratio [1–8]. However, to fully realize the advantages of flexible electronics, equally flexible energy storage devices, capable of sustaining their electrochemical performance under different deformation states, need to be developed [1,2,5,6,8–10].

Currently, supercapacitors are considered as a prospective form of energy storage devices. Compared to conventional lithium-ion batteries, they are endowed with higher power densities and cycle life (up to 100,000 cycles). However, the application of supercapacitors in high-energy devices such as electric vehicles, mobile, and consumer electronics is hindered by their low energy density. In order to address their low energy densities, extensive research efforts have been conducted on the development of high-performance supercapacitor electrode materials such as transition metal oxides [11,12], conducting polymers [13,14], and high surface area activated carbons [15]. The activated carbons possess high surface areas but have reduced electrical conductivity, high equivalent series resistance (ESR) and poor power density [16,17]. Carbon Nanotubes (CNTs) however have been proven to possess the appropriate balance between pore sizes and surface area (50–1315 m^2/g – depending on the number of walls), as well as high electrical conductivity, making them an ideal material to achieve high capacitance [1,7,18–20]. CNTs can be assembled into various formats including fibers [21,22], modified with electroactive polymers [13,23–25] or doped with transition metals [3,26], to achieve high capacitances and energy densities.

* Corresponding author at: Department of Chemical and Environmental Engineering, University of Cincinnati, OH 45221-0012, USA
E-mail address: vesselin.shanov@uc.edu (V. Shanov).

https://doi.org/10.1016/j.jechem.2019.03.005

Plasma functionalization is a technique, which has been used in a variety of research areas. The reactive species in plasma can break bonds on the surface of a material which is significant for their surface chemistry [27]. Plasma treatment, practiced in this work, can produce surface etching, activation, and surface functional groups [28]. Wet chemical methods have been widely used in functionalizing nanotubes [29,30]. However, this treatment requires multi-step reactions to attain the desired functionality and, in most cases, involves strong chemicals, which alter the bulk properties of the nanotube assembly. Atmospheric pressure plasma treatment of nanotubes, on the other hand, serves as a one-step functionalization process, which is more environmentally friendly. Because it is applied to the surface of the nanotubes, it does not alter their bulk properties, and the nature and quantity of the functional species can be controlled by the choices of plasma gases and plasma parameters. CNTs have been plasma treated to purify them, open their tips and change their surface topography [31,32]. The purification of aligned CNTs removes amorphous carbon and other impurities within the CNTs, thus improving their overall performance while opening the tips and increasing their surface area. CNTs, when plasma functionalized, have also been found to enhance the mechanical, electrical and thermal properties of composites [33–38].

It has been previously reported by our research group that plasma functionalization increases the wettability of carbon-based materials [36]. CNTs by nature are hydrophobic and inert, making them unfavorable for specific applications such as in microfluidic devices. Wettability of carbon nanotubes has been altered by changing their chemical composition or structure, and this can be achieved by oxygen plasma functionalization [32,35–37,39–41].

In this work, we present a simple, controlled, and continuous method of altering the surface chemistry of CNT fibers by atmospheric pressure oxygen plasma functionalization, which leads to improvement in the electrochemical properties of the fibers. The oxygen plasma-functionalized CNT fibers (OPFCNT) were found to have better electrochemical performance compared to the pristine CNT fibers due to their enhanced surface area, oxygen-containing functional groups, and increased electrokinetics after plasma treatment. The fabricated fiber electrodes are lightweight and can be used to assemble new kinds of flexible and portable supercapacitors. We also combined the OPFCNT electrode with ionic liquids, 1-ethyl-3-methylimidazolium (EMIMBF4) and 1-ethyl-3-methylimidazolium bis(trifluoromethylsulfonyl)imide (EMIMTFSI), mixed with a polymer- polyvinylidene fluoride-co-hexafluoropropylene (PVDF), to create gel electrolytes that provided high voltage windows of 3.2 V and 2.8 V, respectively for our fiber-supercapacitors. As shown later, the performance of these supercapacitors have been significantly improved compared to devices made from aqueous based gel electrolyte polyvinyl alcohol and sulfuric acid (PVA-H_2SO_4).

2. Experimental

2.1. Fabrication of CNT fiber

Multi-wall carbon nanotube (MWCNT) fibers are derived by dry spinning from vertically aligned 2–3 wall CNTs. The vertically aligned CNTs are grown by chemical vapor deposition (ET 3000 deposition reactor) on a Si wafer with catalysts (Fe, Co, and Al_2O_3 as a buffer layer) deposited on it by physical vapor deposition. Details on the synthesis of spinnable CNT arrays and fiber fabrication practiced in this work have been published elsewhere [21,22]. All fibers were spun from arrays of 2.5 cm width, which pre-determined their diameter of approximately 55 μm (Figs. S1 and S2).

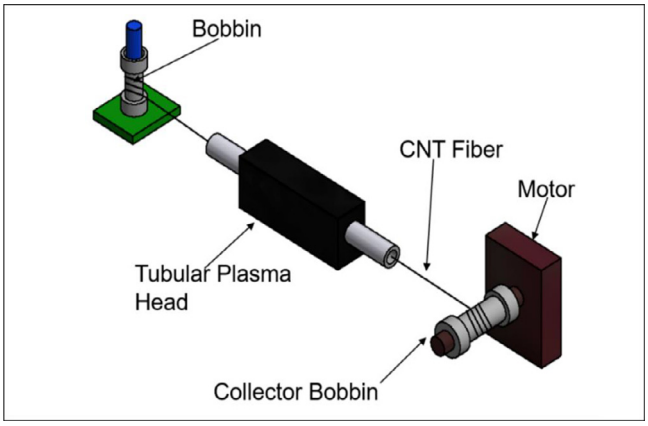

Fig. 1. Tubular plasma head set-up for functionalization of CNT fibers.

Table 1. Plasma parameters employed for the CNT fibers functionalization.

Samples (0.465 cm/s)	Samples (0.206 cm/s)	Power (W)	Oxygen (L/min)
A	A"	60	0.1
B	B"	100	0.3
C	C"	140	0.55

2.2. Functionalization of CNT fibers by oxygen plasma

Oxygen plasma functionalization was conducted by gradually pulling the CNT fiber through a tubular plasma head (Surfx Atomflo 400 system). The set-up is shown in Fig. 1. Pristine CNT fiber was threaded through the plasma head and collected on a bobbin. A constant pulling speed was applied through the plasma head by the collector bobbin, which was motor driven, thus uniformly and reproducibly functionalizing the CNT fiber. The first 30 cm of the collected fiber was not functionalized and served as a reference for comparison.

A separate unit, not shown here, delivered plasma gases (oxygen and helium) and electric power to the plasma head. The varied parameters that have been explored in this process were plasma power (W), the flow rate of oxygen and helium (L/min), and dwell time (the time a fiber is exposed to plasma). For all plasma processing conducted, the amount of helium was kept constant at 15 L/min, according to the recommendation by the manufacturer of the tubular plasma head. The other parameters were chosen to represent 3 levels of plasma functionalization: low, medium and high. The speed of the motor was varied to change the exposure/dwell time of the fibers to the plasma flux and the linear speed of the fiber (fiber velocity) calculated in cm/s.

Table 1 shows the plasma functionalization parameters employed in this work. The plasma parameters increase in harshness from A to C. These parameters were used at two varying speeds of the motor producing two different linear fiber speeds/velocities (0.465 cm/s and 0.206 cm/s). The velocities were calculated from the voltages running the motor, the time corresponding to a complete revolution of the collector bobbin, and the number of revolutions per minute. The speeds, therefore, were limited by the motor used in the set-up and the voltage limit at which it could function properly. Several velocities were tested, however, the best results were seen at 0.465 cm/s and 0.206 cm/s. At 0.206 cm/s, the fibers had a more prolonged exposure time to the plasma and were therefore functionalized to a higher degree than fibers, which were plasma functionalized at 0.465 cm/s. The parameters used in plasma functionalization, as well as the time of exposure, were found to affect the surface chemistry and electrochemistry of the fibers. Table 1 below presents the parameters used for the fibers as well as the nomenclature used in this work.

2.3. Electrode fabrication

All electrodes and devices were made using 7.5 cm long OPFCNT fibers. The tailored fibers were attached to copper tapes with fast drying silver paint (TedPella Inc.). The copper tape served as an electrically conducting lead in the electrochemical analysis arrangement. Three types of device were fabricated by coating the electrodes with three different gel electrolytes: PVA-H_2SO_4, PVDF-EMIMTFSI, and PVDF-EMIMBF4. The PVA-H_2SO_4 was made with 20 mL DI water, 4 mL H_2SO_4 and 2 g PVA. The preparation of the PVDF-EMIMTFSI gel electrolyte included mixing of 2 mL acetone with 0.25 g PVDF and 0.654 mL EMIMTFSI whilst for PVDF-EMIMBF4 we used 2 mL acetone, 0.25 g PVDF and 0.773 mL EMIMBF4. Using ionic liquid electrolytes such as EMIMTFSI and EMIMBF4 increases the operating voltage window of the devices fabricated as compared to the aqueous (H_2SO_4) electrolytes. The coated electrodes after curing were placed in parallel next to each other on a cellulose weighing paper (LabExact) with gel electrolyte between them. Due to the hygroscopic nature of the ionic liquid electrolytes, the devices have been sealed with a "sticky" Kapton tape to keep moisture out. Further experiments are in progress using UV cured polymers to envelope the device. The CNT fiber cores served in this device arrangement as both active electrode materials and the current collector. The polymer gel (PVDF and PVA) provided a dielectric matrix network that also allowed the ions from the electrolyte to flow between the electrodes. Schematic and picture of the fabricated CNT fiber supercapacitor are shown in Fig. S3.

2.4. Characterization and measurements

Electrochemical measurements were carried out with a workstation (Gamry, Interface 1000). The following electrochemical characterization was conducted: cyclic voltammetry at various scan rates, charge-discharge tests, and electrochemical impedance spectroscopy measurements from 10^5 to 10^{-1} Hz applying sinusoidal voltage amplitude of 10 mV at the open circuit potential in 1 M Na_2SO_4. Ag/AgCl was used as the reference electrode, and the counter electrode was made of platinum for the three electrode tests.

The capacitance (C_{device}) of the yarn-supercapacitor device was calculated from the galvanostatic discharge curves at different current densities by using the equation: $C_{device}=I\Delta t/\Delta V$. The gravimetric capacitance (C_m), the areal capacitance (C_A) and volumetric capacitance (C_V) were calculated by the following formula: $C_m = C_{device}/m$, $C_A = C_{device}/A$ and $C_V = C_{device}/V$, respectively. The gravimetric energy density (E_m) and power density (P_m) were calculated by the equations: $E_m = \frac{1}{2} * \frac{C_m(\Delta V)^2}{3.6}$ and $P_m = 3600\frac{E_m}{t}$. The areal energy density (E_A) and power density (P_A) were computed by the expressions: $E_A = \frac{1}{2} * \frac{C_A(\Delta V)^2}{3.6}$ and $P_A = 3600\frac{E_A}{t}$. The volumetric energy density (E_V) and power density (P_V) were calculated by the equations: $E_V = \frac{1}{2} * \frac{C_V(\Delta V)^2}{3.6}$ and $P_V = 3600\frac{E_V}{t}$, where I is the discharge current, t is the discharge time, ΔV is the operating voltage window, m, A and V refer to the mass, area and volume of the device, respectively [39,42,43].

For obtaining the Randles–Sevcik plot, we used a three-electrode test with Ag/AgCl and a platinum wire as the reference and counter electrode, respectively, in an electrolyte solution of 20 mM $K_3[Fe(CN)_6]$ (potassium ferrocyanide) and 0.1 M KCl, where $K_3[Fe(CN)_6]$ served as a redox probe. The peak current can then be evaluated from the Randles-Sevcik equation: $I_P = 2.69 * 10^5 A D^{\frac{1}{2}} n^{\frac{3}{2}} v^{\frac{1}{2}} C$, where $\boldsymbol{C}$ is the concentration of the redox probe used, $\boldsymbol{n}$ is the number of transferred electrons for the redox reaction, $\boldsymbol{D}$ is the diffusivity of potassium ferrocyanide which is 6.67×10^{-6} cm^2 s^{-1}, $\boldsymbol{v}$ is the scan rate, and $\boldsymbol{A}$ is the electrode area. The value of $\boldsymbol{n}$ is equal to one, from the half reaction taking place at the electrode: $Fe(CN)_6^{3-} + e^- \rightarrow Fe(CN)_6^{4-}$ [44,45].

Scanning electron microscopy (SEM) (FEI SCIOS dual beam, 5 kV) and Raman spectroscopy (Renishaw inVia, equipped with a 514 nm Ar-ion laser and a laser spot size of ~1 μm^2) were used to characterize the CNT and OPFCNT fibers. X-ray Photoelectron Spectroscopy (XPS) data were obtained via a VG Thermo-Scientific MultiLab 3000 ultra-high vacuum surface analysis system, with $\sim 10^{-9}$ Torr base pressure using an Al $K\alpha$ source of 1486.6 eV excitation energy. The XPS high-resolution scans for carbon and low-resolution survey scans were taken for each sample on at least two different locations. Specific surface area and pore volumes of outgassed samples were determined by nitrogen adsorption at −196.052 °C on a Micromeritics ASAP 2060 accelerated surface area and porosity measurement system (BET method).

The diameters of the fibers were measured with a Keyence LS-9006 MR High-Accuracy CMOS micrometer. A collector bobbin on a motor pulled the CNT fiber through the device at a constant speed. The device was set to take measurements of the diameter at every second and the data collected was used to plot the diameter vs. length (Fig. S2). From the obtained data, the average diameter of the threads was computed. The masses of the fibers were measured by a Sartorius SE2 ultra-microbalance.

A four-probe setup was employed to quantify the electrical conductivity of the samples. It consists of a Keithley 2182A Nanovoltmeter and a Keithley 6220 precision current source hooked up to a thread holder. This device generates a graph displaying the current vs. voltage over a set range. From this graph, the fiber electrical resistance was calculated. Based on the resistance, diameter, and length of the fiber, its resistivity was computed.

3. Results and discussion

3.1. Electrochemical characterization of plasma functionalized CNT fibers in Na_2SO_4 electrolyte

Fig. 2 presents the data obtained from the three-electrode electrochemical tests on the fiber electrodes. Cyclic voltammetry (CV) curves at 200 mV/s are shown in Fig. S4(a,b) and Fig. 2(a) representing the pristine and functionalized fibers. We found that plasma functionalized fibers revealed significantly larger area enclosed by the CV curve compared to the pristine fiber at the same scan rate. This corresponds to a higher specific capacitance and higher energy density of the OPFCNT fibers. It was also noted that the harshest plasma functionalization parameters in both cases (C and C"), yielded an area enclosed by the CV graph that is smaller to that of samples treated at moderate plasma parameters Fig. S4(a,b). From Fig. 2(a), it is apparent that B" gives greater capacitance compared to B. The only difference between these two fibers is in the exposure time to the plasma flux, which is shorter, for B processed at a greater pulling speed of 0.465 cm/s.

In Fig. S4(c,d) and Fig. 2(b), the Nyquist plots for pristine and plasma treated CNT fibers are presented. Nyquist curves have two main components: a semi-circle in high-frequency regions representing the contact resistance (R_{CT}) between the CNT fiber and the current collector (Cu tape and silver paste) and a vertical line in the low-frequency regions [46]. The real axis intersection with the graph represents the effective series resistance (ESR), which is the internal resistance appearing in series with the device [47]. The total internal resistance is, therefore, a combination of the R_{CT} and ESR within the system.

At a pulling speed through the plasma head of 0.465 cm/s – Fig. S4(c), we noted that all OPFCNT fibers showed less ESR than the pristine CNT. However, at a pulling speed through the plasma head of 0.206 cm/s – Fig. S4(d), only one OPFCNT fiber revealed a

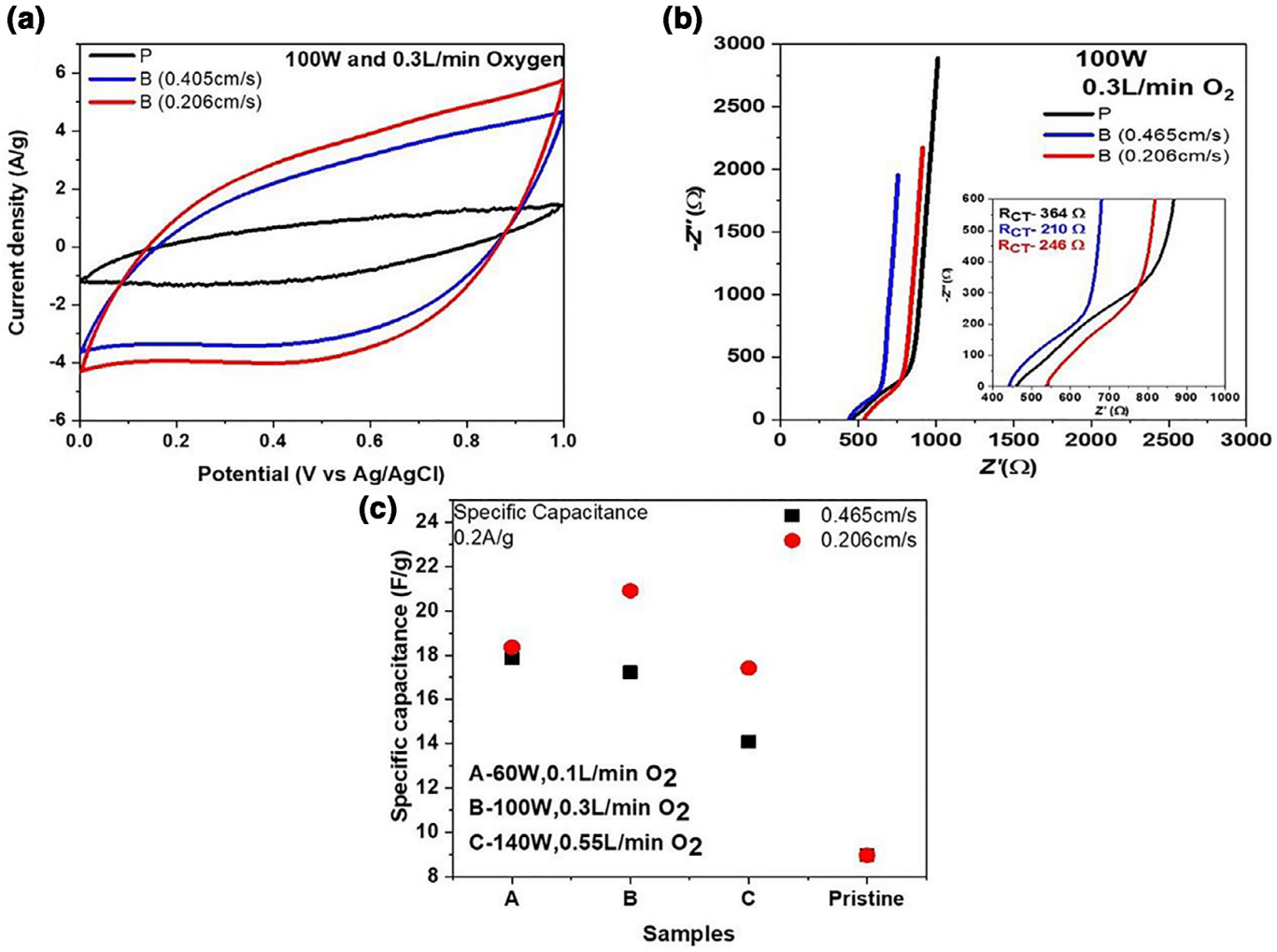

Fig. 2. (a) Cyclic voltammetry at 200 mV/s for plasma functionalized CNT fibers at 100 W, 0.3 L/min of oxygen; (b) Nyquist Plot for plasma functionalized CNT fibers at 100 W, 0.3 L/min of oxygen; (c) Specific capacitances at 0.2 A/g for functionalized CNT fibers; Inset for (b) shows plot intersection with the real axis (ESR).

lower ESR than the pristine one. We attribute the increase in ESR shown by the OPFCNT fiber to the partial damage of the individual CNTs within the fiber caused by the oxygen plasma exposure, as verified by the Raman data. The CNT fibers consist of millions of nanotubes aligned in a uniform direction. These tubes work collectively to transmit phonons and electrons through the fiber. If some of these tubular building blocks of the fibers are damaged, it will hamper the electron transfer along the fiber and will reduce the related amount of current that can be carried through [48]. Harsh plasma functionalization of the fibers can be detrimental to the ion transfer within the fiber since such surface treatment can damage the nanotubes thus hindering the ion transport. These harsh conditions are created by using high plasma parameters (e.g., 140 W, 0.55 L/min O_2).

As displayed in Fig. 2(b), the pristine fiber showed the greatest R_{CT} of approximately 364 Ω compared to B (210 Ω) and B" (246 Ω), respectively. This, when combined with its ESR, produces a greater internal resistance compared to B" and explains why B" has a more significant CV curve area than the pristine fiber – Fig. 2(a), though it has a smaller ESR.

Galvanostatic charge-discharge measurements were also carried out for each CNT fiber at various current densities (Fig. S5). The obtained data were used to calculate the specific capacitance values. From Fig. 2(c), we found that there was an increase in the specific capacitance of the fibers when they were plasma functionalized. The fiber with the highest specific capacitance, obtained at 100 W, 0.3 L/min oxygen and 0.206 cm/s pulling speed, showed an increase of 132.8% in specific capacitance over the pristine fiber (Table S1). This vast improvement is ascribed to the increased wettability and surface area. Carbon-based materials such as the MWCNTs used in this work are generally hydrophobic due to the sp^2 bonding of graphitic carbon. When these materials are used as electrode materials in an aqueous electrolyte system (as described above), the high ionic resistance between the surface of the electrode and aqueous electrolyte hinders the accessibility of the electrolyte ions into the electrode material regardless of its porosity [49,50]. Plasma functionalization has long been confirmed to increase the wettability of CNT and of other carbon-based materials [36,39,40,41,49] (Fig. S6). The surge in hydrophilicity is expected to improve the kinetics of ion transfer within the electric double layer thus causing the observed rise in energy density. The Na^+ and SO_4^{2-} ions from the aqueous electrolyte were, therefore, able to penetrate the electrodes which resulted in the increased area under the CV curves observed in the OPFCNT fibers as well as the increased capacitance data seen [49,50].

3.2. Chemical characterization of plasma functionalized fibers

In a typical Raman spectrum of MWCNT, the main features are the D and G peaks at approximately 1360 cm^{-1} and 1580 cm^{-1},

respectively. The D band reveals defects in the tubes, including sp^3 or single bonded carbon on the surface of the sample. It also exists due to the breathing modes of sp^2 atoms in rings. The G band, on the other hand, is indicative of sp^2 hybridized carbon atoms with double bonds. It is due to the bond stretching of all pairs of sp^2 atoms in both rings and chains [51–56].

Plasma functionalization of CNT fibers results in an intensity increase of the D-band due to the creation of defects in the sample. The peaks in the spectra are normalized to 1, and the I_D/I_G ratios were computed for all samples. Fig. 3(a) and (b) shows Raman spectra of CNT fibers plasma functionalized at pulling speeds of 0.465 cm/s and 0.206 cm/s respectively. Fig. 3(c) displays the I_D/I_G ratios for all samples. The I_D/I_G ratio gives a semi-quantitative measure of the defects created within the fiber due to plasma treatment. OPFCNT fibers treated at 0.206 cm/s pulling speed through the plasma head showed greater I_D/I_G ratio than the fibers plasma functionalized at 0.465 cm/s speed since they had a higher exposure time to the plasma flux. In both cases, sample C revealed the most significant I_D/I_G ratio since it was exposed to the harshest plasma functionalization environment.

Surface analysis of the CNT fibers by X-ray Photoelectron Spectroscopy was conducted to confirm the presence of the created functional groups. XPS peak deconvolution was performed using Shirley-type baseline and pure Gaussian line shape. Fig. 3(d) shows the XPS survey scan of the pristine and B" fibers. The scan proves the presence of carbon and oxygen core peaks at ~284.6 eV and ~532 eV respectively. The OPFCNT fiber (100 W, 0.3 L/min oxygen, 0.206 cm/s) shows an increase in oxygen content from 9.1% in the pristine sample to about 27.5% for the functionalized one. Fig. 3(e) displays the de-convoluted high-resolution multiplex C 1*s* scan of pristine and B" fiber. From the pronounced hump on the spectrum, we observed the presence of C-O-C (ether) and C-OH (hydroxyl) bond at 286.7 eV. The most prominent peak centered at 284.2 eV represents C=C sp^2 hybridized graphitic carbon (C aliphatic). The carbonyl (-C=O-) peak is observed at about 288.1 eV, while the carboxyl (-C=O-O-) peak is seen at 290.2 eV. These results are consistent with previously reported data in the literature [36,57]. Fig. 3(f) presents the de-convoluted O1s scan. The carboxyl (-C=O-O-), hydroxyl (C-OH) and carbonyl peaks are observed at 532 eV, 534.2 eV, and 535 eV, respectively. These results are consistent with previously reported values [58,59].

Temperature Programmed Desorption tests described elsewhere have shown that carbonyl, hydroxyl, and quinone type groups desorb and form CO gas at elevated temperatures, while carboxyl, anhydride and lactone type groups desorb through conversion into CO_2 gas [60,61]. Further research by Teng and co-workers proved that there was a correlation between the increase in capacitance and the rise in oxygen functional groups, which desorbed as CO from the surface of carbon-based electrodes [46,62,63]. They found out that the capacitance contribution by the hydroxyl group on the surface of their carbon-based material was more significant than the capacitance provided by the carboxyl group.

Further research by Andreas and Conway [64], showed that a significant portion of the capacity in C-electrodes is attributed to the pseudocapacitance of quinone surface functionalities and other surface functional groups obtained in acidic and basic media. Therefore, the presence of oxygenated functional groups on the surface of the electrode contributes to increased capacitance by causing a pseudocapacitive effect that enhances Faradaic charge transfer reactions [64,65].

From the deconvoluted peaks discussed earlier (Fig. 3(e) and (f)), we found that the hydroxyl group (C-OH) peak is far higher than the carboxyl group (-C=O-O-) on the surface of the functionalized CNT fiber (100 W, 0.3 L/min oxygen, 0.206 cm/s). Also, the presence of oxygen functional groups on the surface of the OPFCNT fiber is observed. The occurrence of these functional groups and their activities are some of the reasons for the increase in capacitance seen in the three-electrode electrochemical tests presented in Fig. 2.

3.3. Structural characterization of plasma functionalized fibers

Fig. 4(a) and (b) shows SEM images of the pristine fiber and B". CNT fibers fabricated by dry spinning are assembled and maintain good integrity, especially in pristine fiber (Fig. 4(a)) thanks to the van der Waals interaction between the tubes [22]. In fiber B" however, the plasma breaks some bonds in the nanotubes on the surface of the fiber detaching some of the bundles from the bulk material. This causes the hairy appearance shown in Fig. 4(b) compared to the pristine fiber. It also results in decreased load and tensile stress of the fiber (Fig. S7). Fig. 4(c) and (d) offers a larger magnification (20,000×) of the pristine and OPFCNT fiber (B") respectively. From these images, one cannot observe any substantial morphological change in the fibers when compared to one another.

In Fig. 4(e) and (f), cross-sectional SEM images obtained by Focused Ion Beam (FIB) cutting of pristine and B" fibers are presented. Fig. 4(e) reveals uniform porosity in the pristine fiber with the pores evenly distributed across its cross-section. For Fig. 4(f) however, it is apparent that although the core of the fiber is similar in porosity distribution with the pristine fiber, there is a marked difference in the porosity in the outer layer of the fiber (Fig. S8). This may be caused by the plasma functionalization affecting more substantially the surface and the outer shell of the fiber. Since the plasma flux attenuates when penetrating the fiber, its core remains unchanged. This is in agreement with previous work from our group [66] which proved that the plasma functionalization decayed radially in cylindrical objects such as our fibers with diameters greater than 10 μm. For our fibers with approximate diameters of 55 μm, the effect of the plasma was most pronounced in the outer layer of the fibers and not in its core.

UV–vis spectroscopy tests were conducted to ascertain whether the OPFCNT fibers had a greater surface area than the pristine samples. The surface area of the fibers could be evaluated based on the quantity of the methylene blue (MB) dye absorbed [59,67,68]. The fiber with the highest surface area would absorb most of the MB molecules, thus showing the lowest peak intensity on the UV–vis spectrum.

The fibers studied here were selected from the group, which showed the best electrochemical data. Fiber samples 30 cm long were soaked in 3 mL of a 5 mg/L methylene blue (MB) aqueous solution for 19 h in the dark. From the UV–vis spectrum in Fig. 5(a), significantly decreased MB peak intensities (peak located at 665 nm) for plasma functionalized fibers A" (60 W, 0.1 L/min O_2, 0.206 cm/s) and B" (100 W, 0.3 L/min O_2, 0.206 cm/s) were observed compared to pristine CNT fibers. This indicates that more MB dye molecules have been absorbed by the plasma functionalized fibers as compared to the pristine samples. The latter confirms an increase of the ion-accessible surface area for the plasma functionalized fibers used as electrodes [59,67,68].

For most electrochemical capacitors, the capacitance C can be presented as $C = S\varepsilon/d$, where C is the capacitance, S is the electrode surface area, ε is relative permittivity of the solution (medium) and d is the thickness of the double layer [17]. The surface area of the electrode is therefore directly proportional to its capacitance. Using cyclic voltammetry, one can calculate the effective surface area via the Randles-Sevcik equation. Fig. 5(b) displays Randles-Sevcik plots for plasma-functionalized fibers obtained at a pulling speed through the plasma head of 0.206 cm/s. The graphs clearly show an increase in the effective surface area of the OPFCNT fibers compared to the pristine sample. We also observed a reduction in sur-

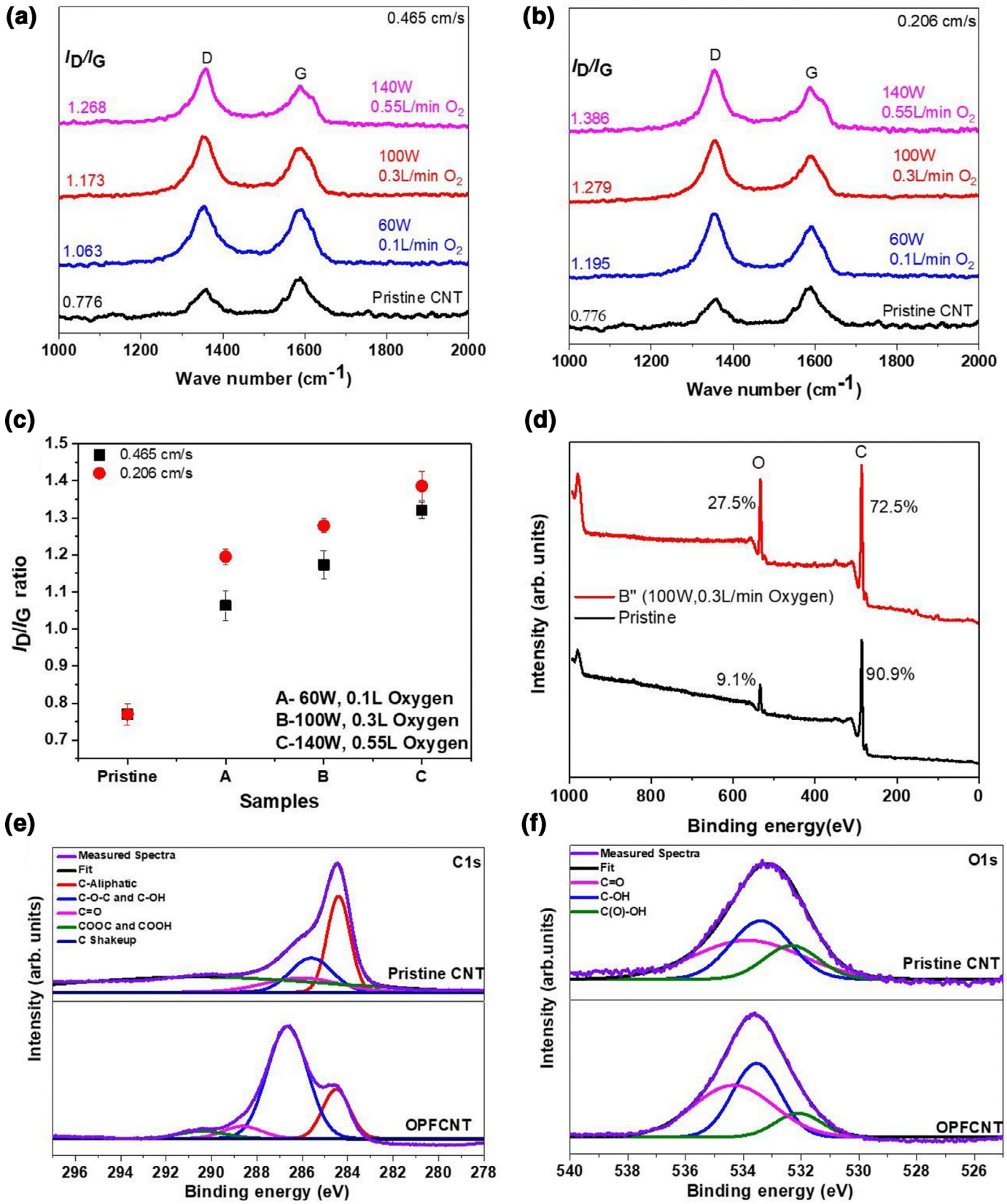

Fig. 3. (a) Raman spectra of oxygen plasma functionalized fibers at a pulling speeds of 0.465 cm/s; (b) Raman spectra of plasma functionalized fibers at a pulling speeds of 0.206 cm/s; (c) Plot of I_D/I_G ratios from the Raman spectra for fibers functionalized at different puling speeds through the plasma head; (d) XPS survey scans of pristine (0 W) and plasma treated CNT fiber (100 W, 0.3 L oxygen, 0.206 cm/s); (e) High-resolution C 1*s* scan of pristine and plasma treated CNT fiber (0.206 cm/s, 100 W, 0.3 L/min oxygen); (f) High-resolution O 1*s* scan of pristine and oxygen plasma treated CNT fiber (0.206 cm/s, 100 W, 0.3 L/min), highlighting different functional groups.

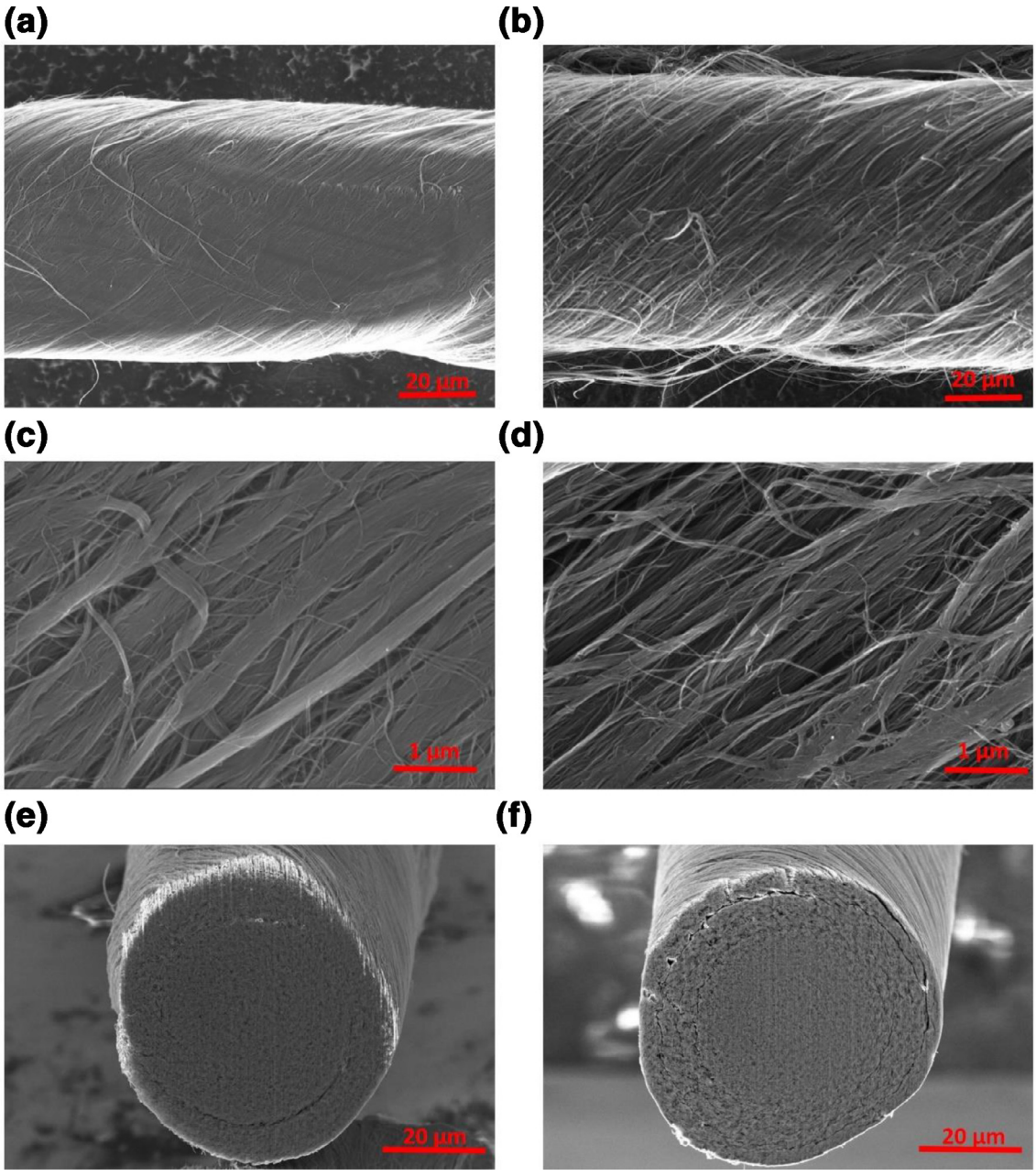

Fig. 4. (a) SEM image of pristine fiber at 1000×; (b) SEM image of fiber B" at 1000×; (c) SEM image of pristine CNT fiber at 20,000×; (d) SEM image of B" at 20,000×; (e) Cross-sectional image of pristine CNT fiber at 1300× obtained by FIB cutting; (f) Cross-sectional image of B" at 1300× obtained by FIB cutting.

face area with the rising of the oxygen plasma functionalization parameters towards harsher values. As a result, the fiber which was plasma functionalized at 140 W, 0.55 L/min O_2 (C") showed the least surface area among all plasma treated fibers.

The BET-determined surface area of B" (208.015 m^2/g) was found to be higher than that of pristine CNT (168.216 m^2/g). This increment in the surface area is attributed to the oxygen plasma functionalization process. The pore characteristics of the fibers were investigated by N_2 adsorption/desorption isotherm tests, and the results are displayed in Fig. 5(c). A type IV isotherm with the characteristic hysteresis loop has been identified from the isotherm tests [69]. The pore size distribution is different for B" and Pristine CNT fibers, as displayed in Fig. 5(d). The microporosity is increased in the B" samples. It is known that micropores enhance the ion storage in carbonaceous materials [70]. From Lozano-Castello et al. [65] demonstrated that capacitance depends on the surface area, pore size distribution, and surface chemistry. It was also shown that the capacitance was higher for samples with wider micropore distribution. There was a strong correlation found between increased capacitance and increased micropores on the surface of the electrodes.

The B" fiber revealed a distribution of 5.45% micropores, 40.47% mesopores, and 54.08% macropores compared to 1.43% micropores, 49.66% mesopores and 48.92% macropores for the pristine CNT fiber, respectively. Fig. 5(e) presents a breakdown of the pore volume percentages of the fibers calculated from the BET data. For each fiber, we computed the proportion of pores in the microporous (0–2 nm), mesoporous (2–50 nm) and the macroporous (>50 nm) range [71]. The mesoporous range is represented here with two subsets 2–10 nm and 10–50 nm.

It was also noted that the pore size distribution of the plasma treated fibers had been changed. The surface area of the pristine CNT fiber has been increased by 23.6% after oxygen plasma functionalization, and the pore sizes generally have been enlarged thus

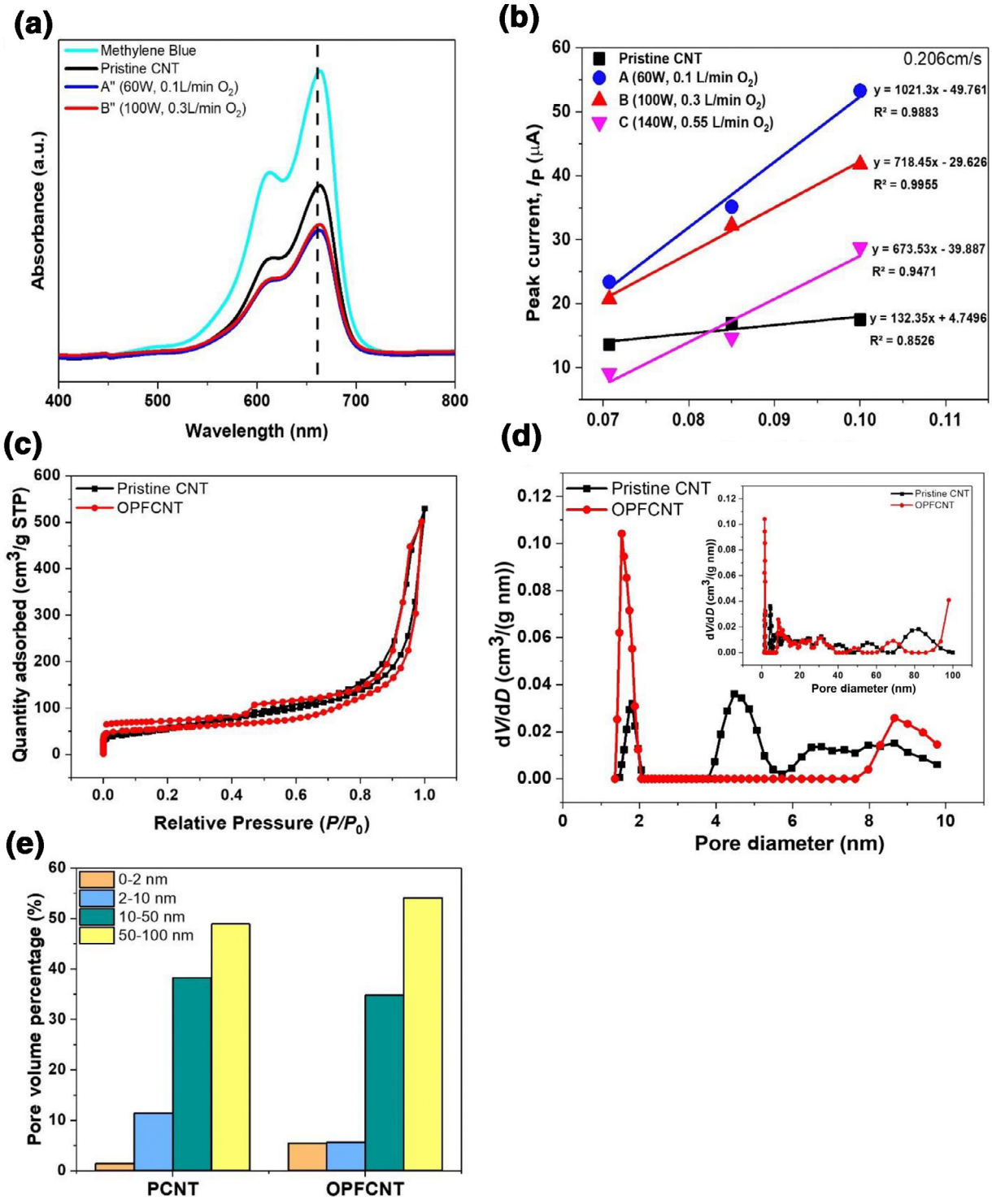

Fig. 5. (a) UV–vis absorption spectra obtained from pristine and plasma functionalized CNT fibers; (b) Randal-Sevcik plot of plasma functionalized CNT fibers acquired at a pulling speed through the plasma head of 0.206 cm/s; (c) Nitrogen adsorption-desorption isotherms for pristine CNT and OPFCNT fibers; (d) Pore size distribution of pristine CNT and OPFCNT fibers; (e) Pore size volume percentages for pristine CNT and OPFCNT fibers.

creating more micropores and macropores. However, a reduction of the mesopore percentage for OPFCNT has been observed in comparison to pristine CNT fibers. The increase in the surface area of the CNT fibers after plasma functionalization stimulates enhanced kinetics of the ion transfer within the electric double layer and further rise of both the energy density and the specific capacitances [72–74].

4. Fiber supercapacitor devices

Fiber supercapacitors fabricated from OPFCNT fibers (100 W, 0.3 L/min O_2 at 0.206 cm/s) with different electrolyte systems have been compared electrochemically to show their applicability and translation into devices. The fibers were used both as current collectors and active materials in the devices fabricated and to

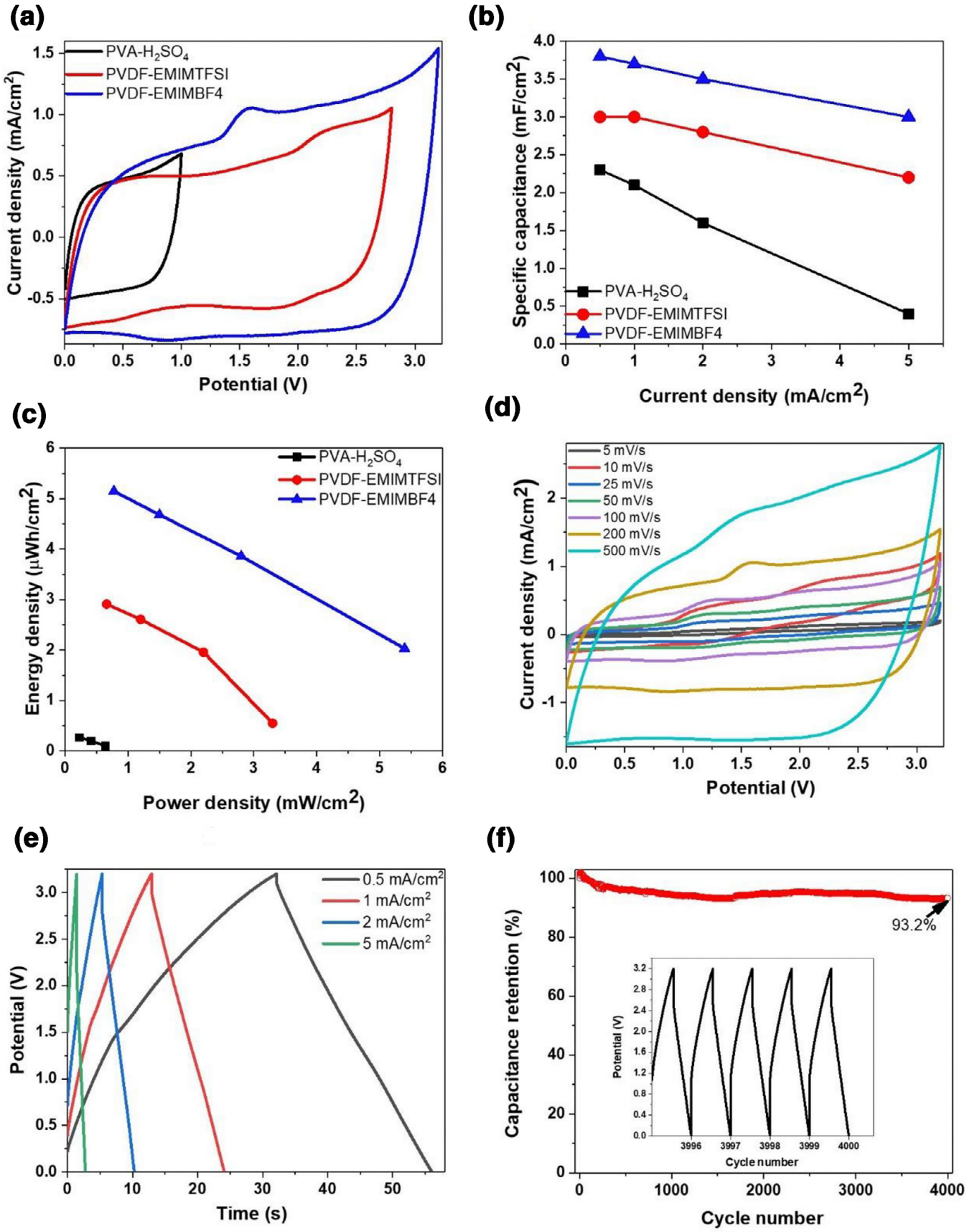

Fig. 6. (a) Cyclic voltammetry curves at 200 mV/s of OPFCNT fiber supercapacitors; (b) Specific capacitances of fiber supercapacitors at different scan rates obtained from the galvanostatic charge-discharge (GCD) tests; (c) Ragone plot of fabricated in this work devices; (d) CV curves at various scan rates for EMIMBF4 device; (e) GCD curves at different current densities for EMIMBF4 device; (f) Cyclic stability for OPFCNT EMIMBF4 device. Inset: galvanostatic charge-discharge curves obtained from testing between 3996 and 4000 cycles.

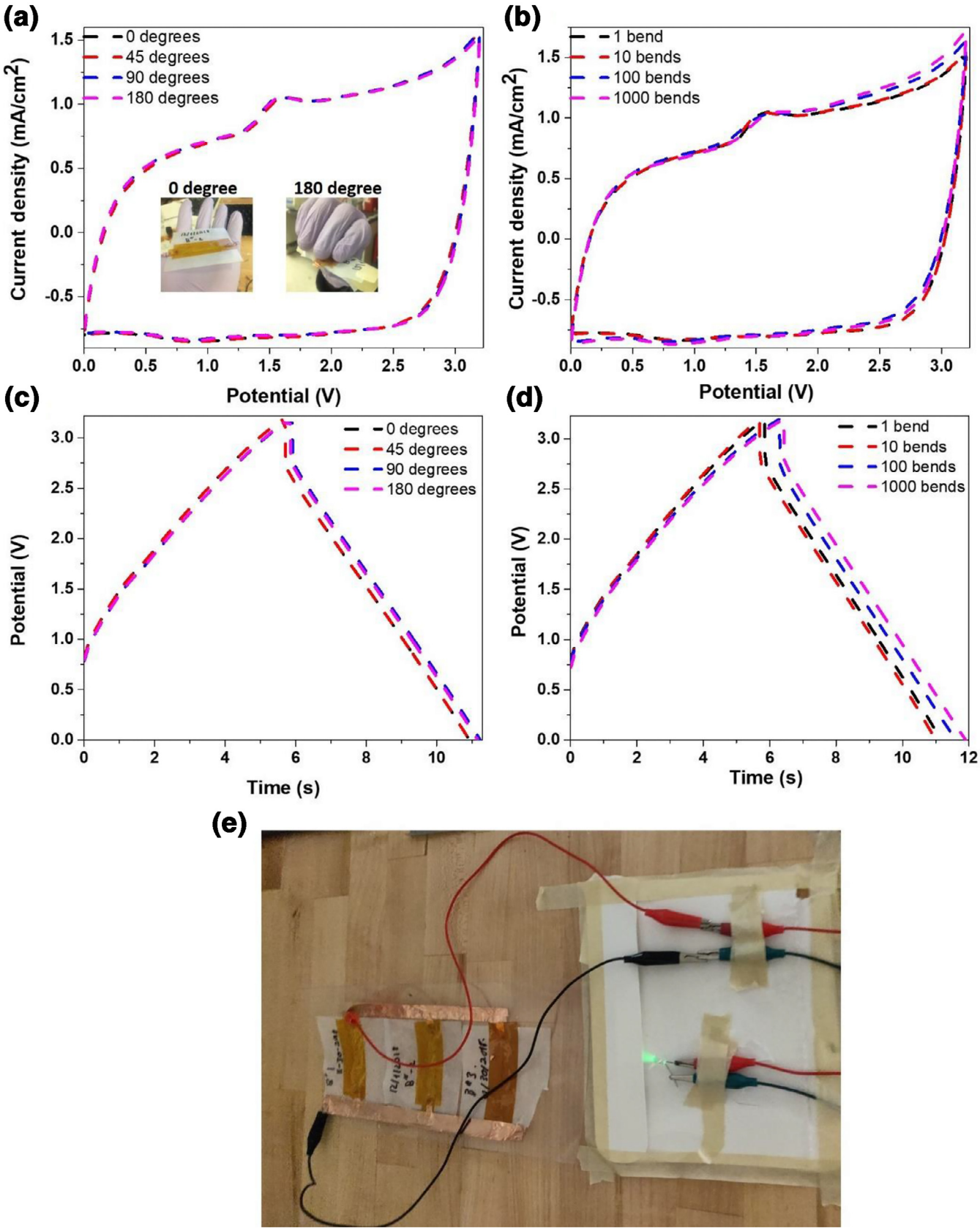

Fig. 7. (a) CV curves of the OPFCNT-EMIMBF4 device tested under different bending angles; (b) CV curves of the OPFCNT-EMIMBF4 device obtained at different number of bends; (c) GCD curves of the OPFCNT-EMIMBF4 device under different bending angles; (d) GCD curves of the OPFCNT-EMIMBF4 device obtained at different number of bends; (e) Digital photo of 3 OPFCNT-EMIMBF4 devices connected in parallel and powering a LED.

evaluate their energy storage properties, a series of electrochemical measurements were performed.

Fig. 6(a) shows cyclic voltammetry curves for the assembled fiber supercapacitors at a scanning rate of 200 mV/s. The curves were quasi-rectangular and had a rapid current response to voltage reversal at the start and end of the voltage window showing a typical behavior of electric double layer capacitors [75]. As expected, the device fabricated with EMIMBF4 gel electrolyte revealed a far greater by area cyclic voltammetry curve than the other devices thus representing a larger capacitance and the best charge-storage capability. Fig. 6(b) shows the areal specific capacitance based on the galvanostatic charge-discharge (GCD) tests at current densities of 0.5–5 mA/cm^2. The EMIMBF4 device demonstrated the highest specific capacitance of all the devices at the different current densities. At 0.5 mA/cm^2, the EMIMBF4 device revealed a specific capacitance, which was 27% and 65% greater than the specific capacitances of the EMIMTFSI and the H_2SO_4 devices, respectively.

Fig. 6(c) presents the Ragone plots for the fabricated devices. The energy density of all the devices followed a downward trend with respect to the power densities. The EMIMBF4 device attained an energy density of 5.15 μWh/cm^2 at a power density of 7.76 W/m^2. The same set of parameters has been computed as 2.91 μWh/cm^2/6.59 W/m^2 for the EMIMTFSI electrolyte device and 0.27 μWh/cm^2/2.27 W/m^2 for the H_2SO_4 device, respectively.

The cyclic voltammetry and GCD data for the EMIMBF4 device are presented in Fig. 6(d) and (e). The device kept its CV shapes at scan rates up to 500 mV/s showing good supercapacitor behavior. Nearly triangular and symmetric charge-discharge curves were also observed with no apparent internal resistance (IR) drop. The slightly nonlinear curve is attributed to the introduction of the oxygen functional groups during the plasma functionalization process.

Fig. 6(f) presents the cycling stability of the OPFCNT EMIMBF4 gel electrolyte device at 2 mA/cm^2 during a galvanostatic charge-discharge over 4000 cycles. The obtained capacitance retention was 93.2%. The inset also shows the galvanostatic charge-discharge curves for testing between 3996 and 4000 cycles. Each of the charge-discharge segment for a single cycle is uniform and attains 3.2 V during the charging process. Overall, the tested device showed excellent stability and cycle life.

The EMIMBF4 devices were subjected to bending at different angles (45°, 90° and 180°) in order to prove their potential application in wearable electronics. Fig. 7(a) and (c) shows CV curves (200 mV/s) and GCD graphs (2 mA/cm^2) of one device during the bending process. The obtained CV and GCD plots maintained their shape and size unchanged at different bending angles thus demonstrating their flexibility. The same EMIMBF4 device was also bent up to 1000 times and the CV and GCD curves at 1, 10, 100 and 1000 number of bends were plotted. The plots presented in Fig. 7(b) and (d) show that the CV and GCD curves retained their shape and size the same when bending the device from 1 up to 1000 cycles. This was another proof that the fabricated energy storage devices can perform with predictable stability under cyclic bending.

In order to verify the practicality and feasibility of the energy storage devices fabricated in this work, three fiber OPFCNT-EMIMBF4 supercapacitors have been wired in parallel and successfully powered a LED, as shown in Fig. 7(e).

5. Conclusions

CNT dry-spun fibers with approximately 55 μm diameters were oxygen plasma functionalized using a continuous and reproducible process. XPS and Raman data proved the controlled amount of functionalization on the surface of the CNT fibers. Electrodes were then fabricated from the functionalized fibers and analyzed electrochemically. Oxygen plasma functionalization was found to increase the specific capacitance of the fiber electrodes by about 132.8% compared to the pristine fiber.

The improved capacitance was attributed to pseudocapacitive effects of the oxygen functional groups, enhanced wettability, alteration of pore sizes and increased surface area of the fibers (confirmed by UV–vis, Randal-Sevcik plots and BET).

The oxygen plasma functionalized fibers were used to create devices with different electrolyte systems. The OPFCNT-EMIMBF4 revealed the best electrochemical properties of all the devices. It performed well under deformation and bending and demonstrated excellent cyclic stability (93.2%) and long performance life. The practical use of these devices was illustrated by successfully powering a LED.

The described and studied approach of oxygen plasma functionalization can be used continuously to process extended lengths of CNT fibers, yarns or ribbons and sheets for improvement of their electrochemical properties.

Acknowledgments

This work was funded by a NASA Grant NNX13AF46A and partly by the National Institute for Occupational Safety and Health through the UC Pilot Research Project Training Program ERC Grant #T42OH008432.

Declaration of interests

None.

Supplementary materials

Supplementary material associated with this article can be found, in the online version, at doi:10.1016/j.jechem.2019.03.005.

References

[1] P. Xu, T. Gu, Z. Cao, B. Wei, J. Yu, F. Li, J.H. Byun, W. Lu, Q. Li, T.W. Chou, Adv. Energy Mater. 4 (2014) 1300759.
[2] J. Bae, M.K. Song, Y.J. Park, J.M. Kim, M. Liu, Z.L. Wang, Angew. Chem. – Int. Ed. 50 (2011) 1683–1687.
[3] C. Choi, J.A. Lee, A.Y. Choi, Y.T. Kim, X. Leprõ, M.D. Lima, R.H. Baughman, S.J. Kim, Adv. Mater. 26 (2014) 2059–2065.
[4] B. Zheng, T. Huang, L. Kou, X. Zhao, K. Gopalsamy, C. Gao, J. Mater. Chem. A 2 (2014) 9736–9743.
[5] V.T. Le, H. Kim, A. Ghosh, J. Kim, J. Chang, Q.A. Vu, D.T. Pham, J.H. Lee, S.W. Kim, Y.H. Lee, ACS Nano 7 (2013) 5940–5947.
[6] X. Zhao, B. Zheng, T. Huang, C. Gao, Nanoscale 7 (2015) 9399–9404.
[7] C. Choi, J.M. Lee, S.H. Kim, S.J. Kim, J. Di, R.H. Baughman, Nano Lett. 16 (2016) 7677–7684.
[8] Y. Fu, H. Wu, S. Ye, X. Cai, X. Yu, S. Hou, H. Kafafy, D. Zou, Energy Environ. Sci. 6 (2013) 805–812.
[9] Y. Fu, X. Cai, H. Wu, Z. Lv, S. Hou, M. Peng, X. Yu, D. Zou, Adv. Mater. 24 (2012) 5713–5718.
[10] X. Xiao, T. Li, P. Yang, Y. Gao, H. Jin, W. Ni, W. Zhan, X. Zhang, Y. Cao, J. Zhong, L. Gong, W.C. Yen, W. Mai, J. Chen, K. Huo, Y.L. Chueh, Z.L. Wang, J. Zhou, ACS Nano 6 (2012) 9200–9206.
[11] F. Su, M. Miao, Nanotechnology 25 (2014) 135401.
[12] X. Xia, J. Tu, Y. Zhang, X. Wang, C. Gu, X.B. Zhao, H.J. Fan, ACS Nano 6 (2012) 5531–5538.
[13] E. Frackowiak, V. Khomenko, K. Jurewicz, K. Lota, F. Béguin, J. Power Sour. 153 (2006) 413–418.
[14] C. Yang, P. Liu, Synth. Met. 160 (2010) 768–773.
[15] S.K. Simotwo, P.R. Chinnam, S.L. Wunder, V. Kalra, Highly Durable, ACS Appl. Mater. Interfaces 9 (2017) 33749–33757.
[16] B.E. Conway, Electrochemical Supercapacitors: Scientific Fundamentals and Technical Applications, Kluwer Academic/Plenum Publishers, New York, 1999.
[17] E. Frackowiak, F. Béguin, Carbon 39 (2001) 937–950.
[18] H. Cheng, Z. Dong, C. Hu, Y. Zhao, Y. Hu, L. Qu, N. Chen, L. Dai, Nanoscale 5 (2013) 3428–3434.
[19] T. Chen, L. Qiu, Z. Yang, Z. Cai, J. Ren, H. Li, H. Lin, X. Sun, H. Peng, Angew. Chem. – Int. Ed. 51 (2012) 11977–11980.
[20] A. Peigney, C. Laurent, E. Flahaut, R.R. Bacsa, A. Rousset, Carbon 39 (2001) 507–514.
[21] S.N. Kanakaraj, N.T. Alvarez, S. Gbordzoe, M.S. Lucas, B. Maruyama, R. Noga, Y.Y. Hsieh, V. Shanov, Mater. Res. Express. 5 (2018) 065036.

[22] N.T. Alvarez, P. Miller, M. Haase, N. Kienzle, L. Zhang, M.J. Schulz, V. Shanov, Carbon 86 (2015) 350–357.
[23] V. Gupta, N. Miura, Electrochim. Acta. 52 (2006) 1721–1726.
[24] K. Wang, Q. Meng, Y. Zhang, Z. Wei, M. Miao, Adv. Mater. 25 (2013) 1494–1498.
[25] R. Malik, L. Zhang, C. McConnell, M. Schott, Y.Y. Hsieh, R. Noga, N.T. Alvarez, V. Shanov, Carbon 116 (2017) 579–590.
[26] J. Ren, L. Li, C. Chen, X. Chen, Z. Cai, L. Qiu, Y. Wang, X. Zhu, H. Peng, Adv. Mater. 25 (2013) 1155–1159.
[27] F.S. Denes, S. Manolache, Prog. Polym. Sci. 29 (2004) 815–885.
[28] C. Zhiqiang, H.L. Lu, J.D. Xiujuan, C. Ying, W. Xungai, Nanotubes and Nanosheets, CRC PressTaylor and Francis Group, 2015, pp. 465–494.
[29] V. Datsyuk, M. Kalyva, K. Papagelis, J. Parthenios, D. Tasis, A. Siokou, I. Kallitsis, C. Galiotis, Carbon 46 (2008) 833–840.
[30] H. Hu, B. Zhao, M.E. Itkis, R.C. Haddon, J. Phys. Chem. B 107 (2003) 13838–13842.
[31] S. Huang, L. Dai, J. Phys. Chem. B 106 (2002) 3543–3545.
[32] C.K. Liu, J.M. Wu, H.C. Shih, Sens. Actuat. B Chem. 150 (2010) 641–648.
[33] F. Hussain, J. Compos. Mater. 40 (2006) 1511–1575.
[34] S.C. Tjong, Mater. Sci. Eng. R Rep. 53 (2006) 73–197.
[35] E.T. Thostenson, C. Li, T.W. Chou, Compos. Sci. Technol. 65 (2005) 491–516.
[36] R. Malik, C. Mcconnell, N.T. Alvarez, M. Haase, S. Gbordzoe, V. Shanov, RSC Adv. 6 (2016) 108840–108850.
[37] J.N. Coleman, U. Khan, W.J. Blau, Y.K. Gun'ko, Carbon 44 (2006) 1624–1652.
[38] R.H. Baughman, A.A. Zakhidov, W.A. de Heer, Science 297 (2002) 787–792.
[39] L.L. Zhang, D. DeArmond, N.T.N.T. Alvarez, R. Malik, N. Oslin, C. McConnell, P.K. Adusei, Y.-Y. Hsieh, V. Shanov, Small 13 (2017) 1603114.
[40] A.O. Lobo, S.C. Ramos, E.F. Antunes, F.R. Marciano, V.J. Trava-Airoldi, E.J. Corat, Mater. Lett. 70 (2012) 89–93.
[41] H. Yu, D. Cheng, T.S. Williams, J. Severino, I.M. De Rosa, L. Carlson, R.F. Hicks, Carbon 57 (2013) 11–21.
[42] K.A. Owusu, L. Qu, J. Li, Z. Wang, K. Zhao, C. Yang, K.M. Hercule, C. Lin, C. Shi, Q. Wei, L. Zhou, L. Mai, Nat. Commun. 8 (2017) 14264.
[43] P.K. Adusei, Y.-Y. Hsieh, N. Kanakaraj, Y. Fang, K. Johnson, N.T. Alvarez, V. Shanov, Science, Technology and Advanced Application of Supercapacitors, T. Sato (Ed.), IntechOpen, 2018, doi:10.5772/intechopen.80487.
[44] Y. Yao, K.-K. Shiu, Anal. Bioanal. Chem. 387 (2007) 303–309.
[45] J. Shi, J.C. Claussen, E.S. McLamore, A. Ul Haque, D. Jaroch, A.R. Diggs, P. Calvo-Marzal, J.L. Rickus, D. Marshall Porterfield, Nanotechnology 22 (2011) 355502.
[46] Y.R. Nian, H. Teng, J. Electroanal. Chem. 540 (2003) 119–127.
[47] R. Kötz, M. Carlen, Electrochim. Acta. 45 (2000) 2483–2498.
[48] S. Gbordzoe, S. Yarmolenko, S. Kanakaraj, M.R. Haase, N.T. Alvarez, R. Borgemenke, P.K. Adusei, V. Shanov, Mater. Sci. Eng. B 223 (2017) 143–152.
[49] P. Dulyaseree, V. Yordsri, W. Wongwiriyapan, Jpn. J. Appl. Phys. 55 (2016) 1–6.
[50] H. Zanin, E. Saito, H.J. Ceragioli, V. Baranauskas, E.J. Corat, Mater. Res. Bull. 49 (2014) 487–493.
[51] A.C. Ferrari, Solid State Commun. 143 (2007) 47–57.
[52] A.C. Ferrari, J.C. Meyer, V. Scardaci, C. Casiraghi, M. Lazzeri, F. Mauri, S. Piscanec, D. Jiang, K.S. Novoselov, S. Roth, A.K. Geim, Phys. Rev. Lett. 97 (2006) 187401.
[53] A.C. Ferrari, J. Robertson, Phys. Rev. B 61 (2000).
[54] F. Tuinstra, J.L. Koenig, J. Chem. Phys. 53 (1970) 1126–1130.
[55] C. Castiglioni, F. Negri, M. Rigolio, G. Zerbi, J. Chem. Phys. 115 (2001) 3769–3778.
[56] R.P. Vidano, D.B. Fischbach, L.J. Willis, T.M. Loehr, Solid State Commun. 39 (1981) 341–344.
[57] N.P. Zschoerper, V. Katzenmaier, U. Vohrer, M. Haupt, C. Oehr, T. Hirth, Carbon 47 (2009) 2174–2185.
[58] D. Rosenthal, M. Ruta, R. Schlögl, L. Kiwi-Minsker, Carbon 48 (2010) 1835–1843.
[59] W. Wang, W. Liu, Y. Zeng, Y. Han, M. Yu, X. Lu, Y. Tong, Adv. Mater. 27 (2015) 3572–3578.
[60] G.S. Szymański, Z. Karpiński, S. Biniak, A. Świątkowski, Carbon 40 (2002) 2627–2639.
[61] C. Moreno-Castilla, J. Rivera-Utrilla, J.P. Joly, M.V. López-Ramón, M.A. Ferro-García, F. Carrasco-Marín, Carbon 33 (1995) 1417–1423.
[62] C.T. Hsieh, H. Teng, Carbon 40 (2002) 667–674.
[63] T.A. Centeno, F. Stoeckli, J. Power Sour. 154 (2006) 314–320.
[64] H.A. Andreas, B.E. Conway, Electrochim. Acta 51 (2006) 6510–6520.
[65] D. Lozano-Castello, D. Cazorla-Amoros, A. Linares-Solano, S. Shiraishi, H. Kurihara, A. Oya, Carbon 41 (2003) 1765–1775.
[66] Q. Yu, N.T. Alvarez, P. Miller, R. Malik, M.R. Haase, M. Schulz, V. Shanov, X. Zhu, Materials (Basel) 9 (2016) 68.
[67] G. Wang, H. Wang, X. Lu, Y. Ling, M. Yu, T. Zhai, Y. Tong, Y. Li, Adv. Mater. 26 (2014) 2676–2682.
[68] S. Mishra, H. Nguyen, P.K. Adusei, Y.-Y. Hsieh, V. Shanov, Surf. Interface Anal. 51 (2018) 290–297.
[69] M. Kruk, M. Jaroniec, Chem. Mater. 13 (2001) 3169–3183.
[70] N. Jäckel, P. Simon, Y. Gogotsi, V. Presser, ACS Energy Lett. 1 (2016) 1262–1265.
[71] K. Kaneko, J. Membr. Sci. 96 (1994) 59–89.
[72] M. Beidaghi, Y. Gogotsi, Energy Environ. Sci. 7 (2014) 867–884.
[73] P. Simon, Y. Gogotsi, Nat. Mater. 7 (2008) 845–854.
[74] W. Lu, L. Dai, Carbon Nanotubes, IntechOpen, 2010, pp. 563–591.
[75] L. Kou, T. Huang, B. Zheng, Y. Han, X. Zhao, K. Gopalsamy, H. Sun, C. Gao, Nat. Commun. 5 (2014) 1–10.